

vesselFM: A Foundation Model for Universal 3D Blood Vessel Segmentation

Bastian Wittmann¹ Yannick Wattenberg²
 Tamaz Amiranashvili^{1,3} Suprosanna Shit¹ Bjoern Menze¹
¹University of Zurich ²ETH Zurich ³Technical University of Munich
 {bastian.wittmann, bjoern.menze}@uzh.ch

Abstract

Segmenting 3D blood vessels is a critical yet challenging task in medical image analysis. This is due to significant imaging modality-specific variations in artifacts, vascular patterns and scales, signal-to-noise ratios, and background tissues. These variations, along with domain gaps arising from varying imaging protocols, limit the generalization of existing supervised learning-based methods, requiring tedious voxel-level annotations for each dataset separately. While foundation models promise to alleviate this limitation, they typically fail to generalize to the task of blood vessel segmentation, posing a unique, complex problem. In this work, we present vesselFM, a foundation model designed specifically for the broad task of 3D blood vessel segmentation. Unlike previous models, vesselFM can effortlessly generalize to unseen domains. To achieve zero-shot generalization, we train vesselFM on three heterogeneous data sources: a large, curated annotated dataset, data generated by a domain randomization scheme, and data sampled from a flow matching-based generative model. Extensive evaluations show that vesselFM outperforms state-of-the-art medical image segmentation foundation models across four (pre-)clinically relevant imaging modalities in zero-, one-, and few-shot scenarios, therefore providing a universal solution for 3D blood vessel segmentation.

1. Introduction and Motivation

Blood vessel segmentation represents a (pre-)clinically relevant task in (bio)medical image analysis as it plays a vital role in analyzing, diagnosing, and treating various vascular disorders, such as stroke [12], cerebral aneurysms [37], viral pneumonia [39], coronary artery disease [57], and Alzheimer’s [50]. Despite advances in medical image analysis, accurate and robust segmentation of fully-connected vasculature in task-specific imaging modalities still remains a challenging problem, especially in 3D. This is primarily due to the complexity introduced by intricate minuscule vascular geometries, as well as significant domain gaps

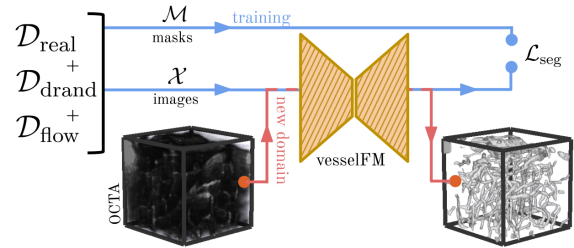


Figure 1. VesselFM is trained in a supervised manner on image-mask pairs from three heterogeneous data sources ($\mathcal{D}_{\text{real}}$, $\mathcal{D}_{\text{drand}}$, and $\mathcal{D}_{\text{flow}}$) and subsequently applied in a zero-, one-, or few-shot fashion to new, unseen 3D blood vessel domains.

caused by imaging modality and protocol-specific variations in signal-to-noise ratios, vascular patterns and scales, imaging artifacts, and background tissues. These variations typically prevent supervised deep learning-based methods from generalizing to unseen 3D blood vessel domains [54]. Consequently, researchers and clinicians find themselves forced to default to the labor-intensive process of acquiring manual, voxel-level consistent annotations from scratch for analyzing vascular images at hand.

Foundation models for image segmentation pre-trained on large-scale datasets have recently emerged as tools that can effortlessly generalize to unseen data distributions [27]. Although foundation models also established themselves in the medical field [35, 53, 61], they typically fail to overcome the unique challenges posed by the task of 3D blood vessel segmentation. To address this limitation, we propose vesselFM, a Foundation Model precisely tailored to universal 3D blood vessel segmentation. We train vesselFM in a supervised manner on image-mask pairs from three heterogeneous data sources (see Fig. 1). To this end, we first curate $\mathcal{D}_{\text{real}}$, which represents, to the best of our knowledge, the largest annotated dataset for 3D blood vessel segmentation, covering a broad range of imaging modalities from various anatomical regions of different organisms. Second, we supplement $\mathcal{D}_{\text{real}}$ with two synthetic data sources, $\mathcal{D}_{\text{drand}}$ and $\mathcal{D}_{\text{flow}}$. In particular, we aim to comprehen-

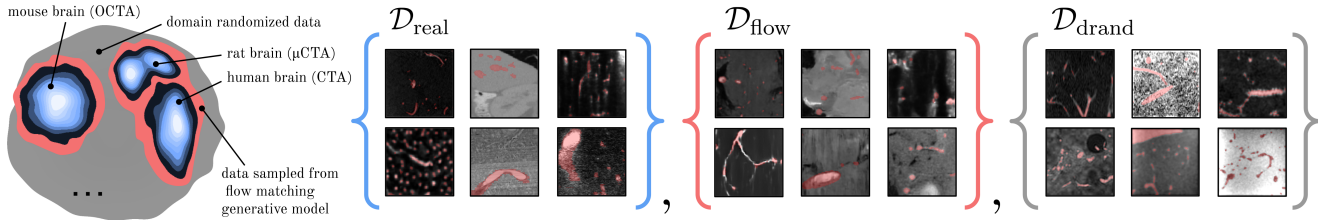


Figure 2. Schematic distributions of our three data sources $\mathcal{D}_{\text{real}}$ (shades of blue), $\mathcal{D}_{\text{flow}}$ (red), and $\mathcal{D}_{\text{drand}}$ (gray). While we aim to comprehensively cover the general domain of 3D vascular images with $\mathcal{D}_{\text{drand}}$, $\mathcal{D}_{\text{flow}}$ effectively broadens the distributions of $\mathcal{D}_{\text{real}}$. Note that segmentation masks are shown in translucent red in the exemplary images.

sively cover the general domain of 3D vascular images by adopting strategies from domain randomization, while we aim to additionally broaden data distributions included in $\mathcal{D}_{\text{real}}$ by sampling from a mask- and class-conditioned flow matching-based generative model (see Fig. 2). Constructing vesselFM on our proposed data sources results in robust features that enable *zero*-shot generalization to unseen domains, facilitating broad clinical use. In extensive experiments, we demonstrate that vesselFM exhibits state-of-the-art performance on the tasks of *zero*-, *one*-, and *few*-shot segmentation across four (pre-)clinically relevant datasets. Our contributions can be summarized as follows:

1. We propose a universal foundation model for 3D blood vessel segmentation, capable of *zero*-shot segmentation. By open-sourcing checkpoints and code, we aim to provide a foundation model that serves as a robust, out-of-the-box tool for researchers and clinicians alike.¹
2. $\mathcal{D}_{\text{real}}$: We curate the largest dataset for 3D blood vessel segmentation, consisting of carefully processed, real 3D vascular images with matching voxel-level annotations.
3. $\mathcal{D}_{\text{drand}}$: We propose an elaborate domain randomization strategy tailored to 3D blood vessel segmentation.
4. $\mathcal{D}_{\text{flow}}$: We introduce mask- and class-conditioned flow matching to 3D medical image generation, producing high-fidelity image-mask pairs that adhere to coherent anatomical constraints.

2. Related Works

In this section, we discuss works closely related to vesselFM and elaborate on how vesselFM distinguished itself from existing literature.

2.1. Foundation Models for Image Segmentation

The advent of the Segment Anything Model (SAM) [27] led to the creation of several SAM-like foundation models aimed at medical image segmentation [35, 52, 62], even in 3D [51, 53, 56, 61]. The general-purpose segmentation model SAM-Med3D [53], *e.g.*, is trained on a combination of 94 datasets, offers generalization across anatom-

ical structures and imaging modalities, and claims *zero*-shot transferability to unseen tasks. In contrast to SAM-Med3D, MedSAM-2 [61] relies on the updated SAM 2 [41] and follows the philosophy of treating 3D medical images as videos, resulting in state-of-the-art results while maintaining exceptional generalization across a wide variety of imaging modalities. VISTA3D [23], on the other hand, is developed specifically for CT scans. VISTA3D segments 127 structures and lesions in highly variant CT scans, offering accurate out-of-the-box results and effortless adaptation to unseen structures. In the realm of vessel segmentation, however, foundation models remain under-explored. Earlier works experimented with fine-tuning models pre-trained on vascular data [24, 46], *few*-shot learning [1], and SAM-like methods tailored to 2D OCTA images [52], 3D vEM images [51], and 2D X-ray images [62]. Unlike vesselFM, all above-mentioned vessel segmentation methods are either limited to specific imaging modalities and anatomical structures or have a significantly narrower scope.

2.2. Synthetic Medical Image Generation

In the medical domain, synthetic data is often used to address data scarcity or enhance data diversity. In this context, deep generative models, with diffusion models at the forefront, have emerged as a powerful technique for producing vast amounts of high-fidelity synthetic data [16, 19]. However, to leverage data generated by diffusion models for the task of segmentation, precisely matching image-mask pairs are required. Tackling this challenge, Med-DDPM [14] and SegGuidedDiff [28] integrate semantic conditioning via channel-wise concatenation of the segmentation mask to the model input, resulting in image-mask pairs following coherent anatomical constraints. While Med-DDPM is tailored to 3D brain imaging synthesis, SegGuidedDiff experiments with 2D breast MRI and abdominal CT generation. The concept of domain randomization [47] represents another promising technique, where fore- and background intensity values and morphological features are randomized in a semi-controlled manner to generate versatile synthetic image-mask pairs that can be utilized to train generalist segmentation models resilient to domain shifts. Billot *et al.* [4]

¹<https://github.com/bwittmann/vesselFM>

Table 1. Overview of $\mathcal{D}_{\text{real}}$, including selected dataset statistics. We estimate the mean shape over the x -, y -, and z -axis individually. The voxel size represents the spatial resolution at acquisition time, while the number of patches reflects the amount of final extracted 128^3 sub-volumes. We further provide an estimate on label quality focusing on vessel connectivity and annotation precision and a brief overview of dataset-specific pre-processing steps, ensuring that datasets comply with our quality standards. Additional details are provided in Suppl. 6. Note that the first four datasets are exclusively used to evaluate vesselFM on unseen domains in our experiments.

	Name	Class c	Tissue Type	Imaging Modality	# Images	Mean Shape	Voxel Size	# Patches	Label Qua.	Pre-Processing**
<i>Evaluation</i>	SMILE-UHURA [9]	1	human brain	MRA	14	$640 \times 482 \times 164$	$0.30 \times 0.30 \times 0.30$ mm	335	9	r, mp
	BvEM [51]	2	mouse brain	vEM	1	$3571 \times 5145 \times 2496$	$0.25 \times 0.25 \times 0.32$ μm	21858	8	r, mp, c
	OCTA [17, 54]	3	mouse brain	OCTA	6	$160 \times 160 \times 160$	$2.00 \times 2.00 \times 2.00$ μm	11	10	-
	MSD8 [2]	4	human liver	CT	443	$512 \times 512 \times 71$	$0.80 \times 0.80 \times 5.00$ mm	2640	9	r, mp, c, ic
	TubeTK [7]	5	human brain	MRA	42	$896 \times 896 \times 257$	$0.50 \times 0.50 \times 0.80$ mm	4116	8	r, mp
		6	mouse liver	HREM MRI	1	$400 \times 400 \times 90$	$0.90 \times 0.90 \times 5.00$ mm	6	6	-
	tUbeNet [24]	7	mouse brain	two-photon microscopy	1	$500 \times 500 \times 357$	$0.20 \times 0.46 \times 5.20$ μm	42	7	r, mp
		8	human brain	CTA	90	$334 \times 451 \times 129$	$0.45 \times 0.45 \times 0.13$ mm	863	8	r, mp
	TopCoW [59]	9	human brain	MRA	90	$406 \times 522 \times 129$	$0.30 \times 0.30 \times 0.60$ mm	1179	8	r, mp
		10	mouse brain	light-sheet microscopy (EB)*	14	$500 \times 500 \times 51$	$2.83 \times 2.83 \times 4.99$ μm	113	7	ic
	VesSAP [48]	11	mouse brain	light-sheet microscopy (WGA)*	14	$500 \times 500 \times 51$	$2.83 \times 2.83 \times 4.99$ μm	113	7	ic
		12	human brain	MRA	40	$544 \times 514 \times 133$	$0.31 \times 0.31 \times 0.60$ mm	726	7	r, mp
	DeepVesselNet [46]	13	rat brain	μCTA	4	$256 \times 256 \times 257$	$0.70 \times 0.70 \times 0.70$ mm	32	7	r, mp
		14	mouse kidney	X-ray	1	$4608 \times 4608 \times 7169$	$1.60 \times 1.60 \times 1.60$ mm	72576	6	mp
	HR-Kidney [29]	15	human liver	CT	20	$512 \times 512 \times 142$	$0.57 \times 0.57 \times 1.60$ mm	352	6	c, mp
	3D-IRCADb-01 [44]	16	mouse brain	multi-photon microscopy	1	$256 \times 256 \times 201$	$1.00 \times 1.00 \times 1.70$ mm	6	8	-
	DeepVess [18]	17	human brain	MRA	45	$1024 \times 1024 \times 93$	$0.26 \times 0.26 \times 0.80$ mm	2070	7	-
		18	mouse brain	light-sheet microscopy	4	$502 \times 2000 \times 2000$	$2.00 \times 2.00 \times 8.00$ μm	3822	6	-
	VesselExpress [45]	19	mouse heart	light-sheet microscopy	3	$223 \times 250 \times 250$	$2.00 \times 2.00 \times 8.00$ μm	19	6	-
		20	mouse bladder	light-sheet microscopy	10	$102 \times 300 \times 300$	$2.00 \times 2.00 \times 8.00$ μm	43	6	-
		21	mouse brain	two-photon microscopy	73	$512 \times 512 \times 44$	$0.70 \times 0.70 \times 5.00$ μm	380	7	-
	MiniVess [40]	22	human kidney	CT	3	$1350 \times 1311 \times 1845$	$2.50 \times 2.50 \times 2.50$ μm	4225	8	-
	HIP-CT [58]	23	mouse brain	light-sheet microscopy	1	$175 \times 170 \times 201$	$6.00 \times 6.00 \times 6.00$ μm	2	9	ic
	LS [5]									

* different dyes used for staining: wheat germ agglutinin (WGA) and Evans blue (EB); ** r: resampled, c: cropped, mp: mask post-processed (e.g., smoothed or multi-class labels to binary), ic: intensities clipped

were the first to adopt a domain randomization strategy for medical image segmentation by proposing SynthSeg, a model capable of segmenting brain MRI scans of varied resolution and contrast. AnyStar [13] extends SynthSeg’s concept to 3D instance segmentation of star-convex shapes such as nuclei, nodules, or metastases. In this work, we leverage both deep generative models and domain randomization strategies to enrich our data sources. Specifically, we extend Med-DDPM by introducing the concept of flow matching [32, 33], which has shown to be superior to diffusion [15, 36], to anatomically controllable vascular image generation, and adapt the concept of domain randomization to 3D blood vessel segmentation.

3. Data Source Generation

We train vesselFM on three heterogeneous data sources: 1) diverse real data ($\mathcal{D}_{\text{real}}$), 2) domain randomized data ($\mathcal{D}_{\text{drand}}$), and 3) data sampled from a flow matching-based generative model ($\mathcal{D}_{\text{flow}}$). Below, we detail each of these three data sources.

3.1. $\mathcal{D}_{\text{real}}$: Diverse Real Data

The development process of generalist foundation models necessitates large-scale, diverse real datasets [8, 35, 53]. To this end, we curate $\mathcal{D}_{\text{real}} = \{\mathcal{X}_{\text{real}}, \mathcal{M}_{\text{real}}\}$, encompassing real images $\mathcal{X}_{\text{real}}$ and their corresponding annotated segmentation masks $\mathcal{M}_{\text{real}}$ (see Table 1 for dataset overview and statistics; Fig. 3 for exemplary images). $\mathcal{D}_{\text{real}}$ comprises 115,461 3D patches of shape 128^3 curated from 17 annotated sources, which we further separate into 23 datasets based on tissue types, imaging modalities, and protocols.

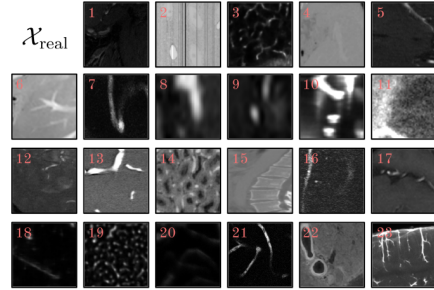


Figure 3. Slices of images $\mathcal{X}_{\text{real}}$ from $\mathcal{D}_{\text{real}}$. $\mathcal{D}_{\text{real}}$ contains 115,461 vascular images of shape 128^3 with matching voxel-level annotations collected from 23 datasets (classes are indicated in red) of diverse imaging modalities, depicting a wide range of anatomical regions from different organisms at various scales.

For ease of reference, each dataset in $\mathcal{D}_{\text{real}}$ is indexed by a unique class $c \in \mathcal{C} = \{1, \dots, 23\}$ (see Table 1, 3rd column). Importantly, $\mathcal{D}_{\text{real}}$ covers a broad array of clinically (e.g., MRA, CTA, and X-ray) and pre-clinically relevant (e.g., vEM, μCTA , and two-photon microscopy) imaging modalities. It integrates data from several anatomical regions (e.g., brain, kidney, and liver) in various organisms (e.g., human, mouse, and rat), thus providing an expansive spectrum of blood vessel patterns of varying structural and functional properties. Further, we deliberately include datasets of the same imaging modalities to bridge domain gaps in, e.g., scale and contrast, induced by high variability in dataset-specific imaging protocols. We pay special attention to solely including datasets that adhere to a high standard in label quality. To curate $\mathcal{D}_{\text{real}}$, we pre-process

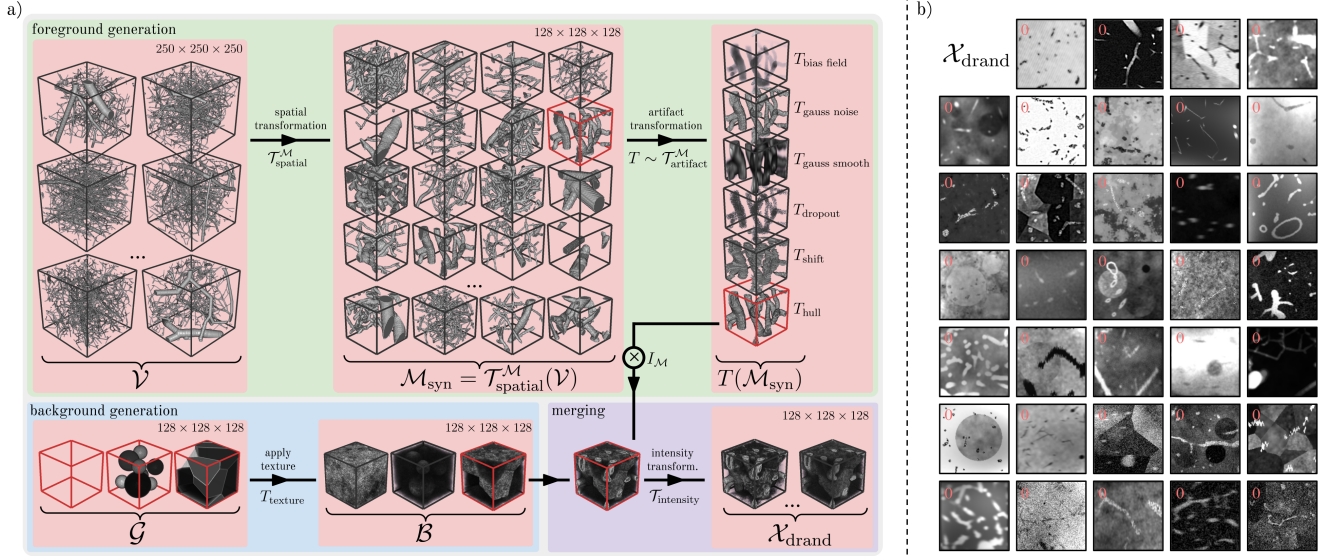


Figure 4. a) Schematic overview of our domain randomized generative pipeline used to generate $\mathcal{D}_{\text{drand}} = \{\mathcal{X}_{\text{drand}}, \mathcal{M}_{\text{syn}}\}$. We specifically highlight its three main components: foreground generation, background generation, and merging. Note that we indicate instances forwarded to the subsequent step in the color red for illustration purposes. b) Slices of exemplary images $\mathcal{X}_{\text{drand}}$, categorized as $c = 0$. The wide variety of generated, highly diverse images showcases the effectiveness of our proposed domain randomization strategy.

each dataset in a similar manner. Specifically, we tile the raw images and their labels into 128^3 patches to conform to our target shape. Additional details on pre-processing can be found in Suppl. 6. To the best of our knowledge, $\mathcal{D}_{\text{real}}$ represents the largest real dataset for the task of 3D blood vessel segmentation to this date.

3.2. $\mathcal{D}_{\text{drand}}$: Domain Randomization

Inspired by recent works [4, 13], we explore the use of domain randomization to generate a massive amount of matching image-mask pairs of semi-randomized style, categorizing them under class $c = 0$. In the following, we describe our proposed domain randomization strategy tailored to 3D blood vessels. An overview of our domain randomized generative pipeline used to create $\mathcal{D}_{\text{drand}} = \{\mathcal{X}_{\text{drand}}, \mathcal{M}_{\text{syn}}\}$ is depicted in Fig. 4. We detail its parametrization in Suppl. 7.

Foreground generation. To generate synthetic masks acting as foreground geometries, we utilize 1,137 vascular patches \mathcal{V} of shape 250^3 provided by Wittmann *et al.* [54]. These vascular patches, originating from graph representations of corrosion casts [49], accurately preserve both general angioarchitectural and morphological properties characteristic of 3D blood vessels with minimal artifacts. Therefore, \mathcal{V} provides the perfect foundation by ensuring functional fidelity, a key requirement for generating realistic vascular images. First, we process \mathcal{V} by applying spatial transformations $\mathcal{T}_{\text{spatial}}^{\mathcal{M}}$. Specifically, we crop with random center positions to the target shape of 128^3 , followed by

random flipping and rotation across all three axes. To ensure robustness against variations in blood vessel scale and density, we subsequently apply random dilation and random zooming. Additionally, we address variations in blood vessel curvature and tortuosity by employing random elastic deformation and binary smoothing. Applying $\mathcal{T}_{\text{spatial}}^{\mathcal{M}}$ results in a broad range of realistic vascular patterns (see Fig. 4a). Throughout this work, we refer to $\mathcal{T}_{\text{spatial}}^{\mathcal{M}}(\mathcal{V})$ as the set \mathcal{M}_{syn} . Next, we emulate a broad range of foreground artifacts present in real vascular images by concluding with carefully selected artifact transformations $\mathcal{T}_{\text{artifact}}^{\mathcal{M}} = \{T_{\text{bias field}}, T_{\text{gauss noise}}, T_{\text{gauss smooth}}, T_{\text{dropout}}, T_{\text{shift}}, T_{\text{hull}}, T_{\text{identity}}\}$ (see Fig. 4a). In contrast to $\mathcal{T}_{\text{spatial}}^{\mathcal{M}}$, which is applied consecutively, we sample a single artifact transformation T from $\mathcal{T}_{\text{artifact}}^{\mathcal{M}}$ for each processed vascular patch.

Background generation. Considering that the interplay of imaging techniques and protocols, background tissue compositions, and, *e.g.*, pathological conditions creates a broad spectrum of background intensity patterns, we model background images \mathcal{B} containing various background geometries of diverse textures. Specifically, we incorporate three variants of background geometries \mathcal{G} (see Fig. 4a). 1) Spheres: we include non-overlapping spheres; 2) polyhedrons: we split the image into polyhedral regions using Voronoi partitioning [3]; 3) none: we do not incorporate any background geometries. For background geometries and the background itself, we sample versatile Perlin noise patterns [13, 38] that accurately mimic textures characteris-

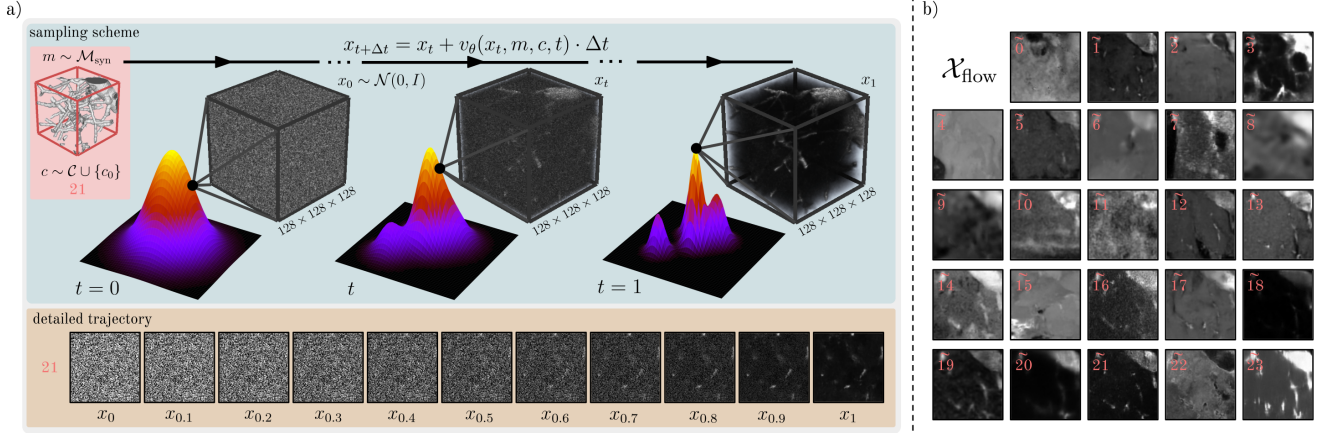


Figure 5. a) Sampling of synthetic images $\mathcal{X}_{\text{flow}}$ via our mask- and class-conditioned flow matching-based generative model. We explicitly show our sampling scheme, mapping a sample $x_0 \sim \mathcal{N}(0, I)$ to an exemplary sample x_1 of class $\hat{21}$. In addition, we present a more detailed trajectory, which is for improved visibility plotted in 2D. b) Slices of exemplary images $\mathcal{X}_{\text{flow}}$, sampled from our generative model. Note that all of the depicted slices are conditioned on the same mask, and we solely vary the class. We would like to emphasize that our generative model is able to produce synthetic images almost indistinguishable from real images (compare with Fig. 3).

tic of vascular images. Further, we also include plain background images consisting of a randomly selected intensity value drawn from $\mathcal{U}(0, 1)$ for enhanced diversity.

Fore- and background merging. Subsequently, we merge $T(\mathcal{M}_{\text{syn}})$ into the background images \mathcal{B} via either voxel-wise addition/subtraction or by replacing background intensity values with mask intensity values. To assign intensities $I_{\mathcal{M}}$ to individual masks that separate them from their respectively matched background images, we estimate mean background intensities $I_{\mathcal{B}}^{\mu}$ and follow $I_{\mathcal{M}} \notin [I_{\mathcal{B}}^{\mu} - \delta, I_{\mathcal{B}}^{\mu} + \delta]$. Lastly, we additionally aim to broaden the domain of the merged images by applying an ample range of intensity transformations $\mathcal{T}_{\text{intensity}}$ with loose configurations. We consecutively perform random bias field augmentations, add Gaussian noise, apply random localized spikes in k-space, randomly adjust the image contrast, perform Gaussian smoothing with either individual or shared σ values for all spatial dimensions, add Rician noise, apply Gibbs noise, perform random Gaussian sharpening, and randomly transform intensity histograms.

3.3. $\mathcal{D}_{\text{flow}}$: Flow Matching-Based Image Generation

Flow matching [32, 33] is a promising alternative to diffusion models and has shown superior performance on natural images [15, 36]. To generate our third data source $\mathcal{D}_{\text{flow}} = \{\mathcal{X}_{\text{flow}}, \mathcal{M}_{\text{syn}}\}$, we train and subsequently sample images from a mask- and class-conditioned flow matching-based generative model \mathcal{F} , aiming at further broadening the distributions of $\mathcal{D}_{\text{real}}$ in a data-driven manner. \mathcal{F} utilizes a θ -parametrized network representing a learned, time-dependent velocity field v , which is trained to map samples

$x_0 \sim \mathcal{N}(0, I)$ to samples x_1 of the data distribution via an ordinary differential equation (ODE):

$$\frac{d}{dt}x_t = v_{\theta}(x_t, m, c, t), \quad (1)$$

where $t \in [0, 1]$ represents the time, c the class we condition on, and m the conditioning mask. To train \mathcal{F} , we optimize the conditional flow matching (CFM) objective [32], which minimizes the L_2 loss between the predicted velocity $v_{\theta}(x_t, m, c, t)$ and the sampled ground truth velocity $u_t(x_t|x_1)$ at time t :

$$\mathcal{L}_{\text{CFM}}(\theta) = \mathbb{E}_{t, x_1, x_t} \|v_{\theta}(x_t, m, c, t) - u_t(x_t|x_1)\|^2. \quad (2)$$

We define the forward process as $x_t = tx_1 + (1-t)x_0$, leading to $u_t(x_t|x_1) = (x_1 - x_t)/(1-t)$ in the loss above. The time-linear forward process provides straighter ODE trajectories than a popular variance-preserving diffusion noise schedule in DDPM, simplifying sampling at inference [32, 33, 36]. We train \mathcal{F} on matching image-mask pairs (x_1, m) and their associated classes $c \in \mathcal{C} \cup \{0\}$, sampled from *both* of our previously generated data sources. Building on anatomically controllable medical image generation methods [14, 28], we implement mask conditioning by concatenating the mask channel-wise with the input image x_t . Class information is incorporated by adding the class embedding to the time embedding, followed by injection into the intermediate feature layers via addition.

To generate $\mathcal{D}_{\text{flow}}$, we ultimately sample a vast amount of images $\mathcal{X}_{\text{flow}}$ (see Fig. 5) by discretizing (1) via Euler integration:

$$x_{t+\Delta t} = x_t + v_{\theta}(x_t, m, c, t) \cdot \Delta t, \quad \Delta t = \frac{1}{N}, \quad (3)$$

Table 2. Quantitative results. We compare vesselFM to state-of-the-art foundation models for medical image segmentation on three tasks: *zero*-, *one*-, and *few*-shot 3D blood vessel segmentation. VesselFM is evaluated on four datasets of clinical (SMILE-UHURA [9], MSD8 [2]) and pre-clinical (OCTA [17, 54], BvEM [51]) relevance and consistently outperforms all baselines by a relatively large margin.

Task	Model	OCTA [17, 54]		BvEM [51]		SMILE-UHURA [9]		MSD8 [2]	
		Dice \uparrow	clDice \uparrow	Dice \uparrow	clDice \uparrow	Dice \uparrow	clDice \uparrow	Dice \uparrow	clDice \uparrow
<i>zero-shot</i>	tUbeNet [24]	36.01	23.64	10.03	11.17	48.32	36.85	5.13	5.84
	VISTA3D [23]	13.60	3.72	0.94	2.03	5.05	1.62	23.83	20.25
	SAM-Med3D [53]	6.74	6.56	5.98	7.38	2.12	1.66	7.94	7.89
	MedSAM-2 [61]	28.56	15.76	10.92	12.27	3.85	5.46	14.53	14.27
	vesselFM (ours)	46.94	67.07	67.49	62.04	74.66	75.27	29.69	36.14
<i>one-shot</i>	tUbeNet [24]	38.09	59.37	10.75	11.53	57.67	53.25	13.66	15.41
	VISTA3D [23]	51.24	25.69	8.25	15.04	56.53	42.42	31.73	32.94
	SAM-Med3D [53]	38.33	54.90	49.47	52.14	38.57	36.94	29.29	36.78
	MedSAM-2 [61]	56.68	50.95	24.07	24.69	19.78	11.87	30.21	23.89
	vesselFM (from scratch)*	65.57	73.79	63.85	39.55	37.99	45.72	27.13	29.48
vesselFM (ours)	72.10	83.73	78.27	79.91	76.43	78.36	36.88	48.65	
<i>few-shot</i>	tUbeNet [24]	41.61	57.98	5.41	10.22	56.31	49.28	17.67	18.97
	VISTA3D [23]	54.25	32.59	24.04	38.10	61.17	51.05	41.90	46.45
	SAM-Med3D [53]	37.85	56.94	57.86	66.04	46.59	44.63	31.30	35.48
	MedSAM-2 [61]	56.96	51.99	18.76	19.66	58.15	42.72	29.24	22.38
	vesselFM (from scratch)*	67.37	75.79	63.03	56.69	50.51	58.77	32.64	36.03
vesselFM (ours)	75.70	84.03	78.11	84.54	78.77	79.37	45.04	57.25	

*Model not pre-trained on $\mathcal{D}_{\text{real}}$, $\mathcal{D}_{\text{drand}}$, and $\mathcal{D}_{\text{flow}}$.

where N represents the total number of time steps. Given that \mathcal{M}_{syn} covers the required range of blood vessel patterns and is devoid of annotator-induced biases and errors in segmentation masks, we opt to exclusively use masks $m \sim \mathcal{M}_{\text{syn}}$ during sampling. For clarity, we use tilde to denote classes of data generated by \mathcal{F} (e.g., $\tilde{7}$).

4. Experiments and Results

In this section, we elaborate on our findings and showcase vesselFM’s performance on three tasks: *zero*-shot, *one*-shot, and *few*-shot segmentation. We evaluate vesselFM on four 3D blood vessel segmentation datasets of unseen clinically (SMILE-UHURA [9], MSD8 [2]) and pre-clinically (OCTA [17, 54], BvEM [51]) relevant domains. In this context, we extract three patches of shape 128^3 from each of these evaluation datasets and use the remaining data for testing and validation (see Suppl. 6 for more details). With the three extracted patches, we define the *one*- and *few*-shot segmentation task as fine-tuning models on either one or all three patches. For *zero*-shot evaluation, we apply models out-of-the-box on the test data without prior fine-tuning. This setup mimics clinical scenarios where annotated data is typically scarce.

We compare vesselFM with four foundation models designed for 3D medical image segmentation, including the generalizable 3D blood vessel segmentation model tUbeNet [24], the CT-specific VISTA3D [23], and the two SAM-like general-purpose segmentation models SAM-Med3D [53] and MedSAM-2 [61]. In our experiments, we exclude the classes of the four datasets used for evaluation (see Table 1, upper section) from the curation of $\mathcal{D}_{\text{real}}$

and $\mathcal{D}_{\text{flow}}$. This results in $\mathcal{D}_{\text{real}}$ containing 90,685 labeled patches. We generate $\mathcal{D}_{\text{flow}}$ by sampling 10,000 image-mask pairs from \mathcal{F} on a single RTX A6000 GPU over the course of three days. To curate $\mathcal{D}_{\text{drand}}$, we sample 500,000 image-mask pairs from our domain randomized generative pipeline. All images-mask pairs are of shape 128^3 . We train vesselFM using all three data sources, with weights assigned roughly according to their sizes (70% $\mathcal{D}_{\text{drand}}$, 20% $\mathcal{D}_{\text{real}}$, and 10% $\mathcal{D}_{\text{flow}}$). We opt for the UNet architecture proposed by Isensee *et al.* [26] to present our segmentation model. For flow matching, we use the UNet from MedDDPM [14] to represent the learned velocity field v . We set the total number of time steps N in (3) to 100. Following common practices, we report Dice scores and topology-aware centerline Dice (clDice) scores [43], which assess the preservation of tubular appearance and connectivity of blood vessels. Further details on our experimental setup can be found in Suppl. 9.

4.1. Quantitative and Qualitative Results

Quantitative results can be observed in Table 2. We find that our proposed foundation model, vesselFM, tailored to universal 3D blood vessel segmentation, outperforms the baseline models on all datasets and tasks by a large margin.

Zero-shot task. VesselFM exhibits exceptional *zero*-shot generalization on all four datasets, which cover a diverse array of unseen domains and even imaging modalities (e.g., OCTA and vEM). Surprisingly, vesselFM scores 5.86 Dice points higher than VISTA3D on MSD8, even though VISTA3D was trained on 11,454 CT volumes, including

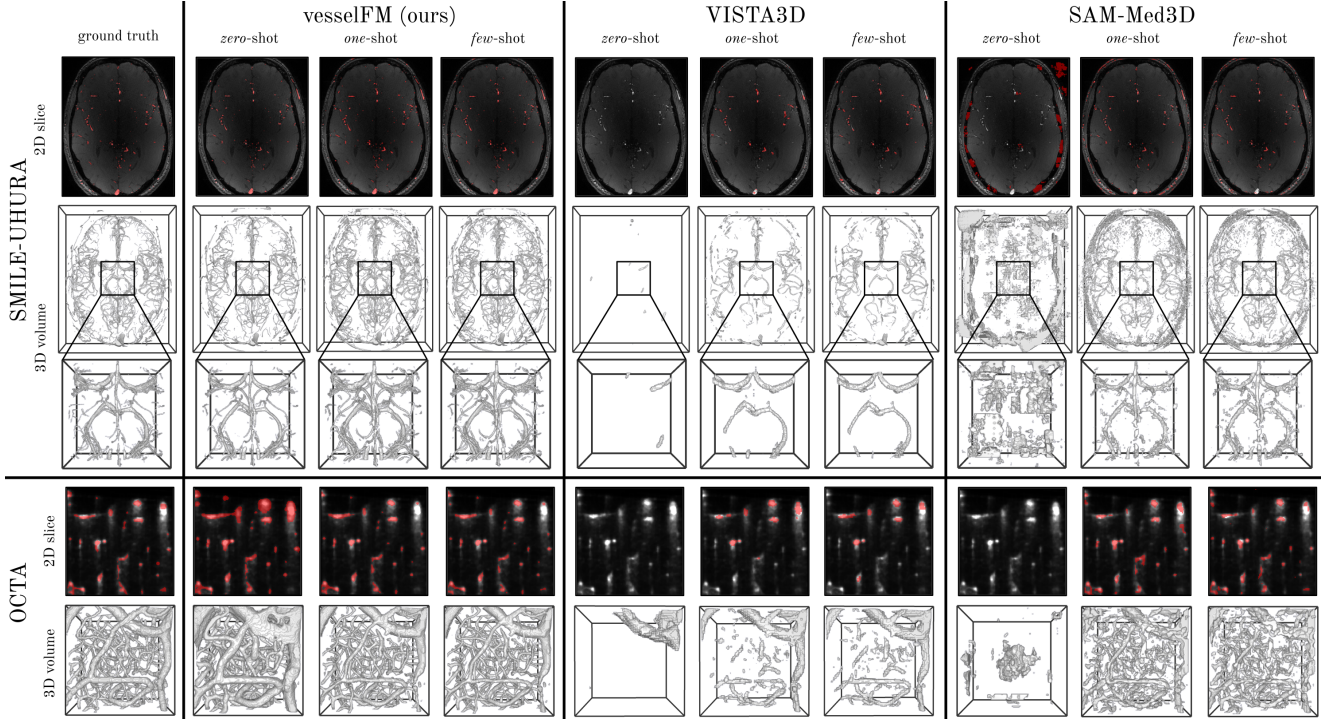


Figure 6. Qualitative results (better viewed zoomed in). We visualize predictions on the SMILE-UHURA and the OCTA datasets for all three tasks (*zero*-, *one*-, and *few*-shot). We compare vesselFM to VISTA3D, SAM-Med3D, and ground truth segmentation masks. Note that vesselFM consistently predicts state-of-the-art results, even in the *zero*-shot setting, demonstrating exceptional generalization to unseen domains. For better visibility, we show a zoomed-in view of the 3D predictions on the SMILE-UHURA datasets.

data from MSD8 itself. This highlights vesselFM’s strong inductive bias, enabled by training on our three proposed heterogeneous blood vessel data sources. Moreover, vesselFM outperforms the generalizable 3D blood vessel segmentation model tUbeNet, trained on four blood vessel datasets of varying imaging modalities. We observe that tUbeNet struggles in more complex imaging modalities where blood vessels do not have a stark contrast to background tissues (*e.g.*, BvEM and MSD8). The general-purpose segmentation models SAM-Med3D and MedSAM-2 both fail to segment blood vessels in the *zero*-shot setting. Notably, vesselFM’s *zero*-shot results surpass *few*-shot results achieved by baseline models on SMILE-UHURA in Dice and cIDice.

One- and few-shot tasks. Fine-tuning vesselFM in a *one*- or *few*-shot manner generally increases segmentation performance. Given that baseline models rely on architectures, which easily overfit to the small amount of training data provided in the *one*- and *few*-shot settings, we additionally compare vesselFM to a variant of the same configuration that is trained from scratch without being pre-trained on our three proposed data sources (see footnote in Table 2). We observe that neglecting our three proposed data sources

causes a notable decrease in Dice and cIDice scores, validating our rationale.

Qualitative results mirror the insights gained from quantitative results. Specifically, we find that vesselFM demonstrates exceptional *zero*-shot generalizations, free of annotator-specific biases (see Fig. 6).

4.2. Ablation Studies

We ablate vesselFM’s design choices on the SMILE-UHURA [9] dataset, targeting human brain vessel segmentation in MRAs, a task of high clinical importance for automated diagnosis of various diseases, such as aneurysms. All ablations are conducted for the *zero*-shot segmentation task, given that *zero*-shot generalization is the most pivotal component of segmentation foundation models.

First, we ablate the relevance of our three proposed data sources, $\mathcal{D}_{\text{real}}$, $\mathcal{D}_{\text{drand}}$, and $\mathcal{D}_{\text{flow}}$ (see Table 3). To this end, we train vesselFM on each data source individually and progressively augment $\mathcal{D}_{\text{real}}$ with $\mathcal{D}_{\text{drand}}$ and $\mathcal{D}_{\text{flow}}$. A more complete ablation of our data sources covering all four evaluation datasets and all tasks can be found in Suppl. 8. We observe that supplementing $\mathcal{D}_{\text{real}}$ with $\mathcal{D}_{\text{drand}}$ and $\mathcal{D}_{\text{flow}}$ results in an impressive increase in Dice and cIDice scores of 9.21 and 11.74, respectively. This highlights that leveraging

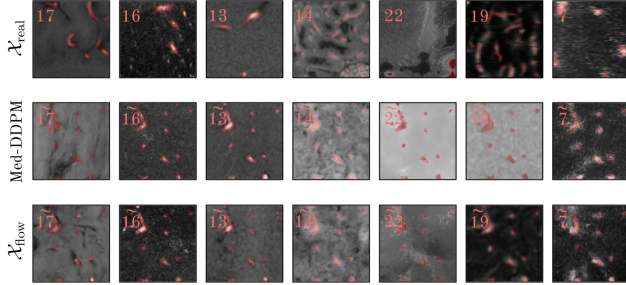


Figure 7. Qualitative comparison of images generated by our flow matching-based generative model \mathcal{F} ($\mathcal{X}_{\text{flow}}$, 3rd row) with images generated by the diffusion-based generative model Med-DDPM [14] (2nd row). We also include real images of the same classes for reference ($\mathcal{X}_{\text{real}}$, 1st row). For improved comparability, we consistently condition \mathcal{F} and Med-DDPM on the same mask m . Segmentation masks are displayed in translucent red.

Table 3. Ablation of data sources.

Data sources	Dice \uparrow	cDice \uparrow
$\mathcal{D}_{\text{real}}$	65.45	63.53
$\mathcal{D}_{\text{real}} + \mathcal{D}_{\text{drand}}$	69.38	72.10
$\mathcal{D}_{\text{real}} + \mathcal{D}_{\text{drand}} + \mathcal{D}_{\text{flow}}$	74.66	75.27
$\mathcal{D}_{\text{drand}}$	55.34	63.16
$\mathcal{D}_{\text{flow}}$	14.33	16.14

all our three proposed heterogeneous data sources collaboratively allows vesselFM to learn robust features that are well-suited for *zero-shot* generalization, enabling a foundation model for universal 3D blood vessel segmentation.

Second, we ablate the design choices of our proposed mask- and class-conditioned flow matching-based generative model \mathcal{F} , used to sample $\mathcal{D}_{\text{flow}}$ (see Table 4). Specifically, we exclude $\mathcal{D}_{\text{drand}}$ from training of \mathcal{F} (2nd row), utilize real masks $\mathcal{M}_{\text{real}}$ instead of our proposed synthetic masks \mathcal{M}_{syn} during sampling from \mathcal{F} (3rd row), and exclude class conditioning (4th row). Subsequently, we replace $\mathcal{D}_{\text{flow}}$ with the respective generated variants and re-train vesselFM. Omitting $\mathcal{D}_{\text{drand}}$, and consequently the class

Table 4. Ablation of mask- and class-conditioned flow matching.

Method used for $\mathcal{D}_{\text{flow}}$	Dice \uparrow	cDice \uparrow
\mathcal{F}	74.66	75.27
\mathcal{F} , no $\mathcal{D}_{\text{drand}}$	71.24	73.93
\mathcal{F} , $\mathcal{M}_{\text{real}}$	70.12	70.84
\mathcal{F} , no class cond.	74.56	74.75
Med-DDPM [14]	70.34	73.35

$c = 0$, from training reduces the Dice score by 3.42. This suggests that the added data diversity and quantity provided by $\mathcal{D}_{\text{drand}}$ enables \mathcal{F} to generate a wider variety of images, thereby facilitating generalization. Generating $\mathcal{D}_{\text{flow}}$ by conditioning on real masks $\mathcal{M}_{\text{real}}$ included in $\mathcal{D}_{\text{real}}$ in-

stead of synthetic masks results in a 4.54 reduction in Dice score. This finding supports our decision to utilize synthetic masks sampled from \mathcal{M}_{syn} , which are, unlike masks from $\mathcal{M}_{\text{real}}$, free of annotator-induced errors and offer greater diversity. We find that omitting class conditioning leads to a modest drop in Dice by 0.10. Finally, we compare \mathcal{F} , relying on the concept of flow matching, to the diffusion-based, generative model Med-DDPM [14] (5th row). \mathcal{F} outperforms Med-DDPM not only quantitatively (4.32 Dice) but also qualitatively (see Fig. 7). Specifically, we observe that Med-DDPM frequently struggles to capture class-specific artifacts accurately, resulting in low-fidelity synthetic images (*e.g.*, see Fig. 7, classes 22 and 19).

Third, we ablate vesselFM’s segmentation model by experimenting with relevant medical 3D segmentation architectures (see Table 5). Our employed UNet variant [26]

Table 5. Ablation of vesselFM’s segmentation model.

Segmentation arch.	Dice \uparrow	cDice \uparrow
UNet [26]	74.66	75.27
SwinUNETR [20]	60.00	53.92
SwinUNETR-V2 [22]	74.54	74.80
UNETR [21]	46.74	40.15
3D UX-Net [30]	49.99	46.31
MedNeXt [42]	56.47	61.95

surpasses transformer-based [20–22] and ConvNeXt [34]-based [30, 42] architectures alike, which accurately represents the current landscape in medical image segmentation.

5. Conclusion and Outlook

In this work, we propose vesselFM, a foundational model for universal 3D blood vessel segmentation. VesselFM is capable of accurately segmenting 3D vasculature in previously unseen modalities and tissue types in *zero-*, *one-*, and *few-shot* settings, outperforming state-of-the-art medical image segmentation foundational models across all datasets and tasks by a wide margin. We enable *zero-shot* generalization by training vesselFM on three proposed heterogeneous data sources ($\mathcal{D}_{\text{real}}$, $\mathcal{D}_{\text{drand}}$, and $\mathcal{D}_{\text{flow}}$), which we extensively ablate in our experiments. Given that vesselFM pushes the frontier in the (pre-)clinically relevant task of 3D blood vessel segmentation, we hope that our work will enable more precise analysis of vascular disorders and foster more accurate diagnostic tools, ultimately resulting in improved patient outcomes. We advise future work to broaden the scope of vesselFM to other tubular structures (*e.g.*, neurons, airways, or spinal cords) and experiment with tailored post-processing steps to improve blood vessel connectivity, potentially at the graph level [55]. Given that our foundation model is currently constrained to binary blood vessel segmentation, which may be viewed as a limitation, we further aim to extend it to multi-class segmentation tasks.

Acknowledgments: This work was supported by the Helmut Horten Foundation. *TubeTK dataset*: The MR brain images from healthy volunteers used in this paper were collected and made available by the CASILab at The University of North Carolina at Chapel Hill and were distributed by the MIDAS Data Server at Kitware, Inc.

References

- [1] Mumu Aktar, Hassan Rivaz, Marta Kersten-Oertel, and Yiming Xiao. VesselShot: Few-shot learning for cerebral blood vessel segmentation. In *International Workshop on Machine Learning in Clinical Neuroimaging*, pages 46–55. Springer, 2023. 2
- [2] Michela Antonelli, Annika Reinke, Spyridon Bakas, Keyvan Farahani, Annette Kopp-Schneider, Bennett A Landman, Geert Litjens, Bjoern Menze, Olaf Ronneberger, Ronald M Summers, et al. The Medical Segmentation Decathlon. *Nature communications*, 13(1):4128, 2022. 3, 6, 1, 2, 5
- [3] Franz Aurenhammer. Voronoi diagrams—a survey of a fundamental geometric data structure. *ACM Computing Surveys (CSUR)*, 23(3):345–405, 1991. 4
- [4] Benjamin Billot, Douglas N Greve, Oula Puonti, Axel Thielscher, Koen Van Leemput, Bruce Fischl, Adrian V Dalca, Juan Eugenio Iglesias, et al. SynthSeg: Segmentation of brain MRI scans of any contrast and resolution without retraining. *Medical image analysis*, 86:102789, 2023. 2, 4
- [5] Nadine Felizitas Binder, Mohamad El Amki, Chaim Glück, William Middleham, Anna Maria Reuss, Adrien Bertolo, Patrick Thurner, Thomas Deffieux, Chryso Lambride, Robert Epp, et al. Leptomeningeal collaterals regulate reperfusion in ischemic stroke and rescue the brain from futile recanalization. *Neuron*, 112(9):1456–1472, 2024. 3, 1
- [6] brain-development.org. IXI Dataset. <http://brain-development.org/ixi-dataset/>, n.d. 3
- [7] Elizabeth Bullitt, Donglin Zeng, Guido Gerig, Stephen Aylward, Sarang Joshi, J Keith Smith, Weili Lin, and Matthew G Ewend. Vessel Tortuosity and Brain Tumor Malignancy: A Blinded Study. *Academic radiology*, 12(10):1232–1240, 2005. 3, 1
- [8] Victor Ion Butoi, Jose Javier Gonzalez Ortiz, Tianyu Ma, Mert R Sabuncu, John Guttag, and Adrian V Dalca. Uni-seg: Universal Medical Image Segmentation. In *Proceedings of the IEEE/CVF International Conference on Computer Vision*, pages 21438–21451, 2023. 3
- [9] Soumick Chatterjee, Hendrik Mattern, Marc Dörner, Alessandro Sciarra, Florian Dubost, Hannes Schnurre, Rupali Khatun, Chun-Chih Yu, Tsung-Lin Hsieh, Yi-Shan Tsai, et al. SMILE-UHURA Challenge—Small Vessel Segmentation at Mesoscopic Scale from Ultra-High Resolution 7T Magnetic Resonance Angiograms. *arXiv preprint arXiv:2411.09593*, 2024. <https://doi.org/10.7303/syn47164761>. 3, 6, 7, 1, 5
- [10] Ying Chen, Darui Jin, Bin Guo, and Xiangzhi Bai. Attention-Assisted Adversarial Model for Cerebrovascular Segmentation in 3D TOF-MRA Volumes. *IEEE Transactions on Medical Imaging*, 41(12):3520–3532, 2022. 3
- [11] MICrONS Consortium, J Alexander Bae, Mahaly Baptiste, Caitlyn A Bishop, Agnes L Bodor, Derrick Brittain, JoAnn Buchanan, Daniel J Bumbarger, Manuel A Castro, Brendan Celii, et al. Functional connectomics spanning multiple areas of mouse visual cortex. *BioRxiv*, pages 2021–07, 2021. 6
- [12] Aditi Deshpande, Nima Jamilpour, Bin Jiang, Patrik Michel, Ashraf Eskandari, Chelsea Kidwell, Max Wintermark, and Kaveh Laksari. Automatic Segmentation, Feature Extraction and Comparison of Healthy and Stroke Cerebral Vasculature. *NeuroImage: Clinical*, 30:102573, 2021. 1
- [13] Neel Dey, Mazdak Abulnaga, Benjamin Billot, Esra Abaci Turk, Ellen Grant, Adrian V Dalca, and Polina Golland. AnyStar: Domain randomized universal star-convex 3D instance segmentation. In *Proceedings of the IEEE/CVF Winter Conference on Applications of Computer Vision*, pages 7593–7603, 2024. 3, 4
- [14] Zolnamar Dorjsembe, Hsing-Kuo Pao, Sodontavilan Odonchimed, and Furen Xiao. Conditional Diffusion Models for Semantic 3D Brain MRI Synthesis. *IEEE Journal of Biomedical and Health Informatics*, 2024. 2, 5, 6, 8
- [15] Patrick Esser, Sumith Kulal, Andreas Blattmann, Rahim Entezari, Jonas Müller, Harry Saini, Yam Levi, Dominik Lorenz, Axel Sauer, Frederic Boesel, et al. Scaling Rectified Flow Transformers for High-Resolution Image Synthesis. In *Forty-first International Conference on Machine Learning*, 2024. 3, 5
- [16] Paul Friedrich, Yannik Frisch, and Philippe C Cattin. Deep Generative Models for 3D Medical Image Synthesis. *arXiv preprint arXiv:2410.17664*, 2024. 2
- [17] Lukas Glandorf, Bastian Wittmann, Jeanne Droux, Chaim Glück, Bruno Weber, Susanne Wegener, Mohamad El Amki, Rainer Leitgeb, Bjoern Menze, and Daniel Razansky. Bessel beam optical coherence microscopy enables multiscale assessment of cerebrovascular network morphology and function. *Light: Science & Applications*, 13(1):307, 2024. 3, 6, 1
- [18] Mohammad Haft-Javaherian, Linjing Fang, Victorine Muse, Chris B Schaffer, Nozomi Nishimura, and Mert R Sabuncu. Deep convolutional neural networks for segmenting 3D in vivo multiphoton images of vasculature in Alzheimer disease mouse models. *PloS one*, 14(3):e0213539, 2019. 3
- [19] Ibrahim Ethem Hamamci, Sezgin Er, Anjany Sekuboyina, Enis Simsar, Alperen Tezcan, Ayse Gulnihani Simsek, Sevval Nil Esirgun, Furkan Almas, Irem Dogan, Muhammed Furkan Dasdelen, et al. GenerateCT: Text-Conditional Generation of 3D Chest CT Volumes. *arXiv preprint arXiv:2305.16037*, 2023. 2
- [20] Ali Hatamizadeh, Vishwesh Nath, Yucheng Tang, Dong Yang, Holger R Roth, and Daguang Xu. Swin UNETR: Swin Transformers for Semantic Segmentation of Brain Tumors in MRI Images. In *International MICCAI brainlesion workshop*, pages 272–284. Springer, 2021. 8
- [21] Ali Hatamizadeh, Yucheng Tang, Vishwesh Nath, Dong Yang, Andriy Myronenko, Bennett Landman, Holger R Roth, and Daguang Xu. UNETR: Transformers for 3D Medical Image Segmentation. In *2022 IEEE/CVF Winter Con-*

- ference on Applications of Computer Vision (WACV), pages 1748–1758. IEEE, 2022. 8
- [22] Yufan He, Vishwesh Nath, Dong Yang, Yucheng Tang, Andriy Myronenko, and Daguang Xu. SwinUNETR-V2: Stronger Swin Transformers with Stagewise Convolutions for 3D Medical Image Segmentation. In *International Conference on Medical Image Computing and Computer-Assisted Intervention*, pages 416–426. Springer, 2023. 8
- [23] Yufan He, Pengfei Guo, Yucheng Tang, Andriy Myronenko, Vishwesh Nath, Ziyue Xu, Dong Yang, Can Zhao, Benjamin Simon, Mason Belue, et al. VISTA3D: Versatile Imaging Segmentation and Annotation model for 3D Computed Tomography. *arXiv preprint arXiv:2406.05285*, 2024. 2, 6, 3
- [24] Natalie Holroyd, Zhongwang Li, Claire Walsh, Emmeline Brown, Rebecca Shipley, and Simon Walker-Samuel. tUbe net: a generalisable deep learning tool for 3D vessel segmentation. *bioRxiv*, pages 2023–07, 2023. 2, 3, 6, 1
- [25] Tristan T Hormel, David Huang, and Yali Jia. Artifacts and artifact removal in optical coherence tomographic angiography. *Quantitative Imaging in Medicine and Surgery*, 11(3): 1120, 2021. 6
- [26] Fabian Isensee, Paul F Jaeger, Simon AA Kohl, Jens Petersen, and Klaus H Maier-Hein. nnU-Net: a self-configuring method for deep learning-based biomedical image segmentation. *Nature methods*, 18(2):203–211, 2021. 6, 8
- [27] Alexander Kirillov, Eric Mintun, Nikhila Ravi, Hanzi Mao, Chloe Rolland, Laura Gustafson, Tete Xiao, Spencer Whitehead, Alexander C Berg, Wan-Yen Lo, et al. Segment anything. In *Proceedings of the IEEE/CVF International Conference on Computer Vision*, pages 4015–4026, 2023. 1, 2
- [28] Nicholas Konz, Yuwen Chen, Haoyu Dong, and Maciej A Mazurowski. Anatomically-Controllable Medical Image Generation with Segmentation-Guided Diffusion Models. In *International Conference on Medical Image Computing and Computer-Assisted Intervention*, pages 88–98. Springer, 2024. 2, 5
- [29] Willy Kuo, Diego Rossinelli, Georg Schulz, Roland H Wenger, Simone Hieber, Bert Müller, and Vartan Kurtcuoglu. Terabyte-scale supervised 3D training and benchmarking dataset of the mouse kidney. *Scientific Data*, 10(1):510, 2023. 3, 1
- [30] Ho Hin Lee, Shunxing Bao, Yuankai Huo, and Bennett A. Landman. 3D UX-Net: A Large Kernel Volumetric ConvNet Modernizing Hierarchical Transformer for Medical Image Segmentation. In *The Eleventh International Conference on Learning Representations*, 2023. 8
- [31] Yuntao Li and Jianbo Tang. Blood vessel tail artifacts suppression in optical coherence tomography angiography. *Neurophotonics*, 9(2):021906–021906, 2022. 6
- [32] Yaron Lipman, Ricky T. Q. Chen, Heli Ben-Hamu, Maximilian Nickel, and Matthew Le. Flow Matching for Generative Modeling. In *The Eleventh International Conference on Learning Representations*, 2023. 3, 5
- [33] Xingchao Liu, Chengyue Gong, and Qiang Liu. Flow Straight and Fast: Learning to Generate and Transfer Data with Rectified Flow. *arXiv preprint arXiv:2209.03003*, 2022. 3, 5
- [34] Zhuang Liu, Hanzi Mao, Chao-Yuan Wu, Christoph Feichtenhofer, Trevor Darrell, and Saining Xie. A ConvNet for the 2020s. In *Proceedings of the IEEE/CVF conference on computer vision and pattern recognition*, pages 11976–11986, 2022. 8
- [35] Jun Ma, Yuting He, Feifei Li, Lin Han, Chenyu You, and Bo Wang. Segment anything in medical images. *Nature Communications*, 15(1):654, 2024. 1, 2, 3
- [36] Nanye Ma, Mark Goldstein, Michael S Alberg, Nicholas M Boffi, Eric Vanden-Eijnden, and Saining Xie. SiT: Exploring Flow and Diffusion-Based Generative Models with Scalable Interpolant Transformers. In *Computer Vision – ECCV 2024*, 2024. 3, 5
- [37] Hidehisa Nishi, Nicole M Cancelliere, Ariana Rustici, Guillaume Charbonnier, Vanessa Chan, Julian Spears, Thomas R Marotta, and Vitor Mendes Pereira. Deep learning-based cerebral aneurysm segmentation and morphological analysis with three-dimensional rotational angiography. *Journal of NeuroInterventional Surgery*, 16(2):197–203, 2024. 1
- [38] Ken Perlin. An image synthesizer. *ACM Siggraph Computer Graphics*, 19(3):287–296, 1985. 4
- [39] Julien Poletti, Michael Bach, Shan Yang, Raphael Sexauer, Bram Stieltjes, David C Rotzinger, Jens Bremerich, Alexander Walter Sauter, and Thomas Weikert. Automated lung vessel segmentation reveals blood vessel volume redistribution in viral pneumonia. *European Journal of Radiology*, 150:110259, 2022. 1
- [40] Charissa Poon, Petteri Teikari, Muhammad Febrian Rachmadi, Henrik Skibbe, and Kullervo Hynynen. A dataset of rodent cerebrovasculature from in vivo multiphoton fluorescence microscopy imaging. *Scientific Data*, 10(1):141, 2023. 3
- [41] Nikhila Ravi, Valentin Gabeur, Yuan-Ting Hu, Ronghang Hu, Chaitanya Ryali, Tengyu Ma, Haitham Khedr, Roman Rädle, Chloe Rolland, Laura Gustafson, et al. SAM 2: Segment Anything in Images and Videos. *arXiv preprint arXiv:2408.00714*, 2024. 2
- [42] Saikat Roy, Gregor Koehler, Constantin Ulrich, Michael Baumgartner, Jens Petersen, Fabian Isensee, Paul F Jaeger, and Klaus H Maier-Hein. MedNeXt: Transformer-driven Scaling of ConvNets for Medical Image Segmentation. In *International Conference on Medical Image Computing and Computer-Assisted Intervention*, pages 405–415. Springer, 2023. 8
- [43] Suprosanna Shit, Johannes C Paetzold, Anjany Sekuboyina, Ivan Ezhov, Alexander Unger, Andrey Zhylyka, Josien PW Pluim, Ulrich Bauer, and Bjoern H Menze. cDice - a Novel Topology-Preserving Loss Function for Tubular Structure Segmentation. In *Proceedings of the IEEE/CVF conference on computer vision and pattern recognition*, pages 16560–16569, 2021. 6
- [44] Luc Soler, Alexandre Hostettler, Vincent Agnus, Arnaud Charnoz, J Fasquel, Johan Moreau, A Osswald, Mourad Bouhadjar, and Jacques Marescaux. 3D image reconstruction for comparison of algorithm database: A patient specific anatomical and medical image database. *IRCAD, Strasbourg, France, Tech. Rep*, 1(1), 2010. 3, 1

- [45] Philippa Spangenberg, Nina Hagemann, Anthony Squire, Nils Förster, Sascha D Krauß, Yachao Qi, Ayan Mohamud Yusuf, Jing Wang, Anika Grüneboom, Lennart Kowitz, et al. Rapid and fully automated blood vasculature analysis in 3D light-sheet image volumes of different organs. *Cell Reports Methods*, 3(3), 2023. [3](#)
- [46] Giles Tetteh, Velizar Efremov, Nils D Forkert, Matthias Schneider, Jan Kirschke, Bruno Weber, Claus Zimmer, Marie Piraud, and Björn H Menze. DeepVesselNet: Vessel Segmentation, Centerline Prediction, and Bifurcation Detection in 3-D Angiographic Volumes. *Frontiers in Neuroscience*, 14:592352, 2020. [2](#), [3](#), [1](#)
- [47] Josh Tobin, Rachel Fong, Alex Ray, Jonas Schneider, Wojciech Zaremba, and Pieter Abbeel. Domain Randomization for Transferring Deep Neural Networks from Simulation to the Real World. In *2017 IEEE/RSJ international conference on intelligent robots and systems (IROS)*, pages 23–30. IEEE, 2017. [2](#)
- [48] Mihail Ivinov Todorov, Johannes Christian Paetzold, Oliver Schoppe, Giles Tetteh, Suprosanna Shit, Velizar Efremov, Katalin Todorov-Völgyi, Marco Düring, Martin Dichgans, Marie Piraud, et al. Machine learning analysis of whole mouse brain vasculature. *Nature methods*, 17(4):442–449, 2020. [3](#), [1](#)
- [49] Thomas Wälchli, Jeroen Bisschop, Arttu Miettinen, Alexandra Ulmann-Schuler, Christoph Hintermüller, Eric P Meyer, Thomas Krucker, Regula Wälchli, Philippe P Monnier, Peter Carmeliet, et al. Hierarchical imaging and computational analysis of three-dimensional vascular network architecture in the entire postnatal and adult mouse brain. *Nature protocols*, 16(10):4564–4610, 2021. [4](#)
- [50] Konrad W Walek, Sabina Stefan, Jang-Hoon Lee, Pooja Puttigampala, Anna H Kim, Seong Wook Park, Paul J Marchand, Frederic Lesage, Tao Liu, Yu-Wen Alvin Huang, et al. Near-lifespan longitudinal tracking of brain microvascular morphology, topology, and flow in male mice. *Nature Communications*, 14(1):2982, 2023. [1](#)
- [51] Jia Wan, Wanhua Li, Atmadeep Banerjee, Jason Ken Adhinarta, Evelina Sjostedt, Jingpeng Wu, Jeff Lichtman, Hanspeter Pfister, and Donglai Wei. TriSAM: Tri-Plane SAM for zero-shot cortical blood vessel segmentation in VEM images. *arXiv preprint arXiv:2401.13961*, 2024. [2](#), [3](#), [6](#), [1](#)
- [52] Chengliang Wang, Xinrun Chen, Haojian Ning, and Shiyang Li. SAM-OCTA: A Fine-Tuning Strategy for Applying Foundation Model OCTA Image Segmentation Tasks. In *ICASSP 2024-2024 IEEE International Conference on Acoustics, Speech and Signal Processing (ICASSP)*, pages 1771–1775. IEEE, 2024. [2](#)
- [53] Haoyu Wang, Sizheng Guo, Jin Ye, Zhongying Deng, Junlong Cheng, Tianbin Li, Jianpin Chen, Yanzhou Su, Ziyang Huang, Yiqing Shen, Bin Fu, Shaoting Zhang, Junjun He, and Yu Qiao. SAM-Med3D: Towards General-purpose Segmentation Models for Volumetric Medical Images. *arXiv preprint arXiv:2310.15161*, 2024. [1](#), [2](#), [3](#), [6](#)
- [54] Bastian Wittmann, Lukas Glandorf, Johannes C Paetzold, Tamaz Amiranashvili, Thomas Wälchli, Daniel Razansky, and Bjoern Menze. Simulation-Based Segmentation of Blood Vessels in Cerebral 3D OCTA Images. In *International Conference on Medical Image Computing and Computer-Assisted Intervention*, pages 645–655. Springer, 2024. [1](#), [3](#), [4](#), [6](#)
- [55] Bastian Wittmann, Johannes C Paetzold, Chinmay Prabhakar, Daniel Rueckert, and Bjoern Menze. Link Prediction for Flow-Driven Spatial Networks. In *Proceedings of the IEEE/CVF Winter Conference on Applications of Computer Vision*, pages 2472–2481, 2024. [8](#)
- [56] Junde Wu, Wei Ji, Yuanpei Liu, Huazhu Fu, Min Xu, Yanwu Xu, and Yueming Jin. Medical SAM Adapter: Adapting Segment Anything Model for Medical Image Segmentation. *arXiv preprint arXiv:2304.12620*, 2023. [2](#)
- [57] Zhanchao Xian, Xiaoqing Wang, Shaodi Yan, Dahao Yang, Junyu Chen, and Changnong Peng. Main Coronary Vessel Segmentation Using Deep Learning in Smart Medical. *Mathematical Problems in Engineering*, 2020(1):8858344, 2020. [1](#)
- [58] Ekin Yagis, Shahab Aslani, Yashvardhan Jain, Yang Zhou, Shahrokh Rahmani, Joseph Brunet, Alexandre Bellier, Christopher Werlein, Maximilian Ackermann, Danny Jonigk, et al. Deep Learning for Vascular Segmentation and Applications in Phase Contrast Tomography Imaging. *arXiv preprint arXiv:2311.13319*, 2023. [3](#)
- [59] Kaiyuan Yang, Fabio Musio, Yihui Ma, Norman Juchler, Johannes C Paetzold, Rami Al-Maskari, Luciano Höher, Hongwei Bran Li, Ibrahim Ethem Hamamci, Anjany Sekuboyina, et al. Benchmarking the CoW with the TopCoW Challenge: Topology-Aware Anatomical Segmentation of the Circle of Willis for CTA and MRA. *arXiv preprint arXiv:2312.17670*, 2023. [3](#), [1](#)
- [60] Jun Zhu, Marcel T Bernucci, Conrad W Merkle, and Vivek J Srinivasan. Visibility of microvessels in Optical Coherence Tomography angiography depends on angular orientation. *Journal of biophotonics*, 13(10):e202000090, 2020. [6](#)
- [61] Jiayuan Zhu, Yunli Qi, and Junde Wu. Medical SAM 2: Segment medical images as video via Segment Anything Model 2. *arXiv preprint arXiv:2408.00874*, 2024. [1](#), [2](#), [6](#), [4](#)
- [62] Vazgen Zohranyan, Vagner Navasardyan, Hayk Navasardyan, Jan Borggreffe, and Shant Navasardyan. Dr-SAM: An End-to-End Framework for Vascular Segmentation Diameter Estimation and Anomaly Detection on Angiography Images. In *Proceedings of the IEEE/CVF Conference on Computer Vision and Pattern Recognition*, pages 5113–5121, 2024. [2](#)

vesselFM: A Foundation Model for Universal 3D Blood Vessel Segmentation

Supplementary Material

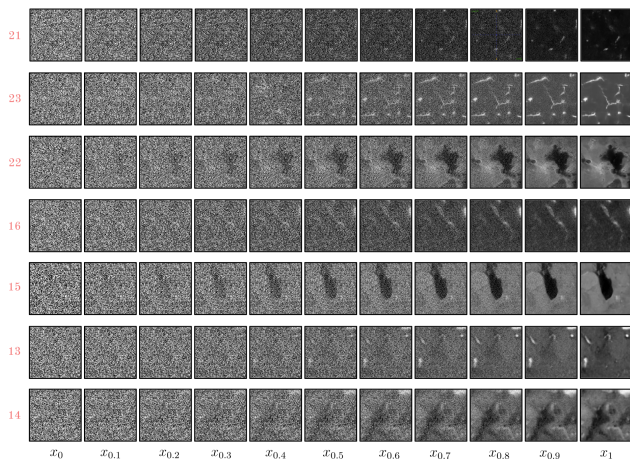


Figure 8. More trajectories of flow matching-based sampling. For improved visibility, we plot 2D slices. Given that the total number of time steps N is set to 100 in our experiments, Δt of 0.1 corresponds to 10 steps. Classes are indicated in red.

6. Pre-Processing of Datasets in $\mathcal{D}_{\text{real}}$

General pre-processing steps. We aim to ensure that all 23 datasets used to curate $\mathcal{D}_{\text{real}}$ (see Table 1) adhere to general vascular imaging characteristics and comply with our label quality standards. To this end, we apply carefully selected pre-processing steps (see Table 1, last column). First, we resample the TubeTK [7], SMILE-UHURA [9], TopCoW [59], MSD8 [2], tUbeNet [24], and DeepVesselNet [46] datasets, establishing appropriate blood vessel scales (e.g., a single vessel should not occupy 90% of the patch) and near-isotropic voxel sizes. In the case of the BvEM [51] dataset, only the labels are resampled, as the annotations were likely made on a downsampled version of the volume. As resampling may introduce label artifacts, we subsequently smooth affected labels using a median filter with a kernel size of 5^3 followed by thresholding (threshold at 0.5). Since the 3D-IRCADb-01 [44] dataset contains labels of multiple structures, we solely keep venous system, artery, and portal vein labels, converting them to binary labels. The original labels of the HR-Kidney [29] dataset are of relatively poor quality. However, enabled by the high signal-to-noise ratio of the volume representing the HR-Kidney dataset, we improve label quality by applying Algorithm 1. To further enhance the visibility of blood vessels, the intensities of the VesSAP [48] and LS [5] datasets are clipped at the 2% and 98% percentiles, while the intensities of the MSD8 dataset are clipped at the 20% and 98% percentiles. We crop the MSD8 and 3D-IRCADb-01 datasets

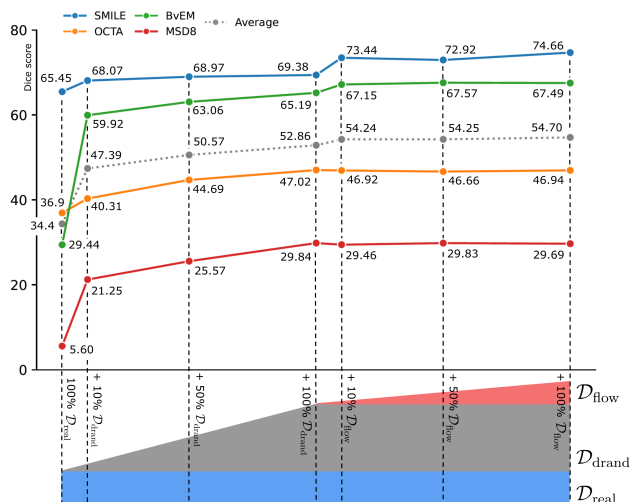


Figure 9. Experiment on the effect of our three proposed data sources on vesselFM’s performance. We gradually augment $\mathcal{D}_{\text{real}}$ with 10%, 50%, and 100% of $\mathcal{D}_{\text{drاند}}$, followed by adding 10%, 50%, and 100% of $\mathcal{D}_{\text{flow}}$ (see bottom part). We report zero-shot Dice scores on the four evaluation datasets. We generally find that augmenting $\mathcal{D}_{\text{real}}$ with $\mathcal{D}_{\text{drاند}}$ and $\mathcal{D}_{\text{flow}}$ results in increased segmentation performance (see average).

to retain only foreground structures, as the images otherwise would primarily consist of non-annotated anatomical structures. Additionally, we crop the borders from the BvEM volume, given that they predominantly contain artifacts.

Algorithm 1 HR-Kidney label improvement.

Input: Image, Intensity Delta = 0.1, Threshold = 0.9, Filter Size = 11

Median \leftarrow MedianFilter(Image, Filter Size)	\triangleright Apply filter to image.
Mask \leftarrow (Image - Median) > Int. Delta	\triangleright Include high local int. variations.
Mask \leftarrow Mask \vee (Image > Threshold)	\triangleright Include high int. values.
Mask \leftarrow Mask \bullet $\mathbf{1}_{5 \times 5 \times 5}$	\triangleright Close small gaps.
Mask \leftarrow RemoveSmallObjects(Mask)	\triangleright Remove small connected components.

\bullet denotes morphological closing.

Evaluation datasets. From each evaluation dataset (see Table 1, upper section), we extract three patches of size 128^3 for fine-tuning models in the *one-* and *few-shot* settings and use the remaining data for testing and validation. *OCTA* [17, 54]: We allocate three of the six samples provided in the OCTA dataset for *one-* and *few-shot* fine-tuning, and reserve the remaining three for model evaluation: two samples for testing and one sample for validation. The three samples used for fine-tuning are center-cropped to adhere to our target shape of 128^3 . *SMILE-UHURA* [9]: The fourteen samples in the SMILE-UHURA

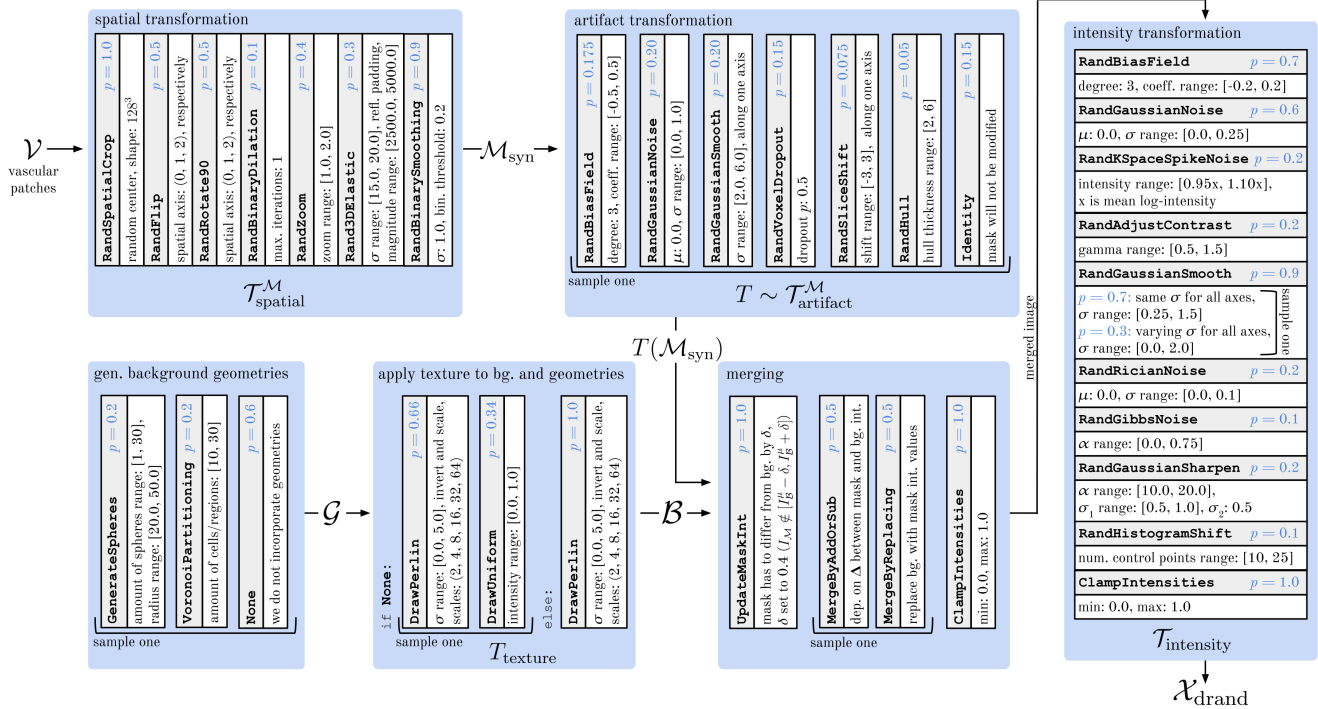


Figure 10. Parametrization of our domain randomized generative pipeline. All parameters were carefully tuned to ensure sufficient diversity while preserving key characteristics relevant to the general domain of vascular images. If not indicated otherwise, all the above transformations are applied consecutively, starting from the left-hand side. Probabilities associated with specific transformations are indicated in blue. Following common practices in medical image analysis, we utilize, whenever possible, transformations from the MONAI framework. Note that we exactly follow the notation from Fig. 4.

dataset are divided into one for validation, ten for testing, and three for extracting patches for fine-tuning. For the extraction of the fine-tuning patches, we pay special attention to extract patches highly representative of the characteristics of MRA scans contained in the SMILE-UHURA dataset (*e.g.*, they contain vasculature, brain tissue, skull, and gyri/sulci). *MSD8* [2]: We split the MSD8 dataset into one validation, 296 test, and three samples utilized to extract patches for fine-tuning. The patches for fine-tuning are chosen from representative regions and padded, if necessary, minimally in the z -dimension using reflective padding to conform to the target shape of 128^3 . *BvEM* [51]: The BvEM dataset contains solely a single volume of shape $3571 \times 5145 \times 2496$. We choose the first 130 slices to extract three 128^3 patches for fine-tuning and one for validation. Then, we leave a buffer of 120 slices to minimize information leakage between the patches used for fine-tuning and testing. Lastly, we extract three bigger test volumes of shape 500^3 from the remaining volume, limiting the overlap of these volumes with the fine-tuning patches in the x - and y -position as much as possible.

7. Parametrization for Domain Randomization

An overview of the parametrization of transformations and operations in our proposed domain randomized generative pipeline, used to generate $\mathcal{D}_{\text{drand}}$, is shown in Fig. 10.

8. More Detailed Ablation of Data Sources

A more detailed ablation study of the effect of supplementing $\mathcal{D}_{\text{real}}$ with $\mathcal{D}_{\text{drand}}$ and $\mathcal{D}_{\text{flow}}$, covering all evaluation datasets and tasks, is shown in Table 6. We find that the combination of all of our three proposed data sources generally yields the best segmentation performance.

To further substantiate this hypothesis, we investigate how the performance of vesselFM scales with the amount of available training data for *zero-shot* segmentation. To this end, we progressively augment $\mathcal{D}_{\text{real}}$ with 10%, 50%, and finally 100% of the data from our two synthetic data sources, $\mathcal{D}_{\text{drand}}$ and $\mathcal{D}_{\text{flow}}$. We scale weights assigned to data sources accordingly. Similar to Table 6, we first augment $\mathcal{D}_{\text{real}}$ with $\mathcal{D}_{\text{drand}}$, followed by $\mathcal{D}_{\text{flow}}$. Our findings are demonstrated in Fig. 9. We observe a significant performance increase introducing $\mathcal{D}_{\text{drand}}$, which flattens as it approaches 100%. On the SMILE-UHURA and BvEM datasets, performance ad-

Table 6. More detailed ablation of supplementing $\mathcal{D}_{\text{real}}$ with $\mathcal{D}_{\text{drand}}$ and $\mathcal{D}_{\text{flow}}$, covering all four evaluation datasets and all tasks. We generally find that the combination of all of our three proposed data sources yields the best segmentation performance.

Task	Model	OCTA [17, 54]		BvEM [51]		SMILE-UHURA [9]		MSD8 [2]	
		Dice \uparrow	cIDice \uparrow	Dice \uparrow	cIDice \uparrow	Dice \uparrow	cIDice \uparrow	Dice \uparrow	cIDice \uparrow
zero-shot	$\mathcal{D}_{\text{real}}$	36.94	57.23	29.44	52.71	65.45	63.53	5.60	8.60
	$\mathcal{D}_{\text{real}} + \mathcal{D}_{\text{drand}}$	47.02	61.05	65.19	65.13	69.38	72.10	29.84	37.47
	$\mathcal{D}_{\text{real}} + \mathcal{D}_{\text{drand}} + \mathcal{D}_{\text{flow}}$	46.94	67.07	67.49	62.04	74.66	75.27	29.69	36.14
one-shot	$\mathcal{D}_{\text{real}}$	69.32	77.68	72.01	85.22	72.20	74.87	27.14	40.51
	$\mathcal{D}_{\text{real}} + \mathcal{D}_{\text{drand}}$	70.63	81.11	75.77	78.48	71.77	71.90	35.35	49.39
	$\mathcal{D}_{\text{real}} + \mathcal{D}_{\text{drand}} + \mathcal{D}_{\text{flow}}$	72.10	83.73	78.27	79.91	76.43	78.36	36.88	48.65
few-shot	$\mathcal{D}_{\text{real}}$	73.01	80.14	67.18	81.41	77.63	77.24	38.65	48.71
	$\mathcal{D}_{\text{real}} + \mathcal{D}_{\text{drand}}$	74.44	82.64	73.43	84.75	77.37	78.28	42.31	54.44
	$\mathcal{D}_{\text{real}} + \mathcal{D}_{\text{drand}} + \mathcal{D}_{\text{flow}}$	75.70	84.03	78.11	84.54	78.77	79.37	45.04	57.25

ditionally spikes after introducing $\mathcal{D}_{\text{flow}}$, while performance on OCTA and MSD8 stagnates. Averaged across all four evaluation datasets (see Fig. 9, average), we find that the additional diversity introduced by $\mathcal{D}_{\text{flow}}$ proves to be consistently beneficial for segmentation performance.

9. More Details on Experimental Setup

Training of vesselFM. We employ a combination of Dice and cross-entropy loss functions, weighted by 0.9 and 0.1, respectively. VesselFM is trained on a single V100 GPU (32GB) with a batch size of 8 until convergence. The learning rate is set to 10^{-4} . We utilize linear warm-up and a cosine annealing learning rate decay to 10^{-6} . During training, we sample classes near uniformly from $\mathcal{D}_{\text{real}}$ and also from $\mathcal{D}_{\text{flow}}$. We solely apply data augmentation to samples from $\mathcal{D}_{\text{real}}$. To optimize training efficiency, we perform data augmentation offline. Specifically, we apply, after extracting 128^3 patches, random flipping and rotation (angle in $[0^\circ, 45^\circ]$) along all axes. Further, we perform random zooming (factor in $[0.9, 1.3]$) and random elastic deformation (σ in $[10, 20]$ and magnitude in $[100, 500]$). Finally, we scale intensities to the range of $[0, 1]$.

One- and few-shot fine-tuning. In the *one-* and *few-shot* setting, we fine-tune vesselFM using a similar setup with an initial learning rate of 10^{-5} decayed to 10^{-7} . We train vesselFM until convergence, selecting the checkpoint with the best Dice scores on the respective validation volume. We apply lightweight data augmentations on the fly: random zooming (factor in $[1, 1.3]$), random shearing (shearing factors in $[0, 0.4]$), random flipping along all axes, random Gaussian noise (μ of 0.3, σ in $[0, 0.5]$), random Gaussian smoothing (σ in $[0, 0.5]$), and random histogram shifting (number of points in $[5, 10]$), followed by intensity scaling.

Following our general procedure, we fine-tune all baselines until convergence and select the checkpoint with the best Dice score on the validation volume for testing. *tUbeNet* [24]: We fine-tune tUbeNet using our training scheme described above, solely adapting the patch size

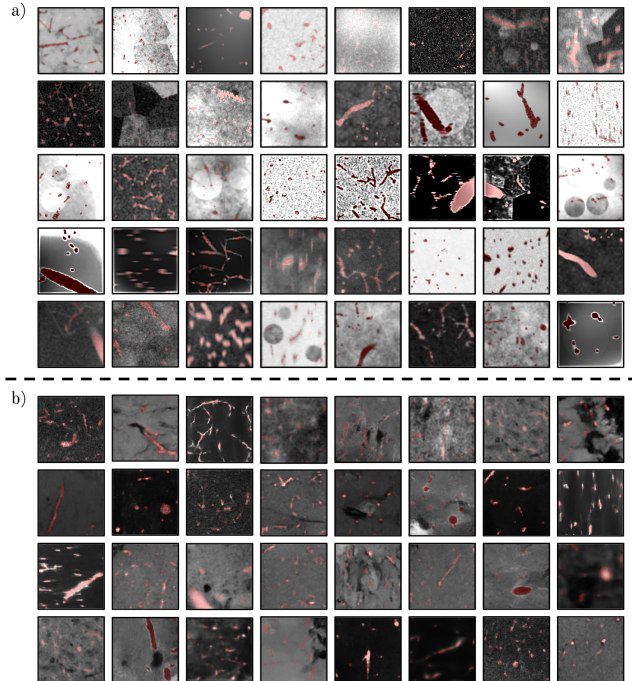


Figure 11. More slices of exemplary images $\mathcal{X}_{\text{drand}}$ (a) and $\mathcal{X}_{\text{flow}}$ (b) with matching masks \mathcal{M}_{syn} shown in translucent red.

(tUbeNet operates on patches of shape 64^3) and employing its linear learning rate decay. We further apply the same lightweight data augmentations used for fine-tuning vesselFM. *VISTA3D* [23]: We fine-tune VISTA3D with the script provided by the authors. As VISTA3D predicts 127 classes, we default to the only class representing blood vessels, the hepatic vessel class. Given that VISTA3D is designed specifically for CT images, we replace their interval-based intensity scaling scheme with a percentile-based scaling scheme (2 and 98 percentiles) and omit their resampling transformation. Further augmentations are left unchanged. During inference, we use the default "auto + point" configuration, which has been shown to yield the best results. *SAM-Med3D* [53]: We adopt SAM-Med3D's

training and inference pipeline without major changes. We utilize their default setting, providing one query point during training and five during inference. Since their data augmentation pipeline closely resembles vesselFM’s, we retain SAM-Med3D’s without alterations. *MedSAM-2* [61]: As MedSAM-2 is trained on images of size 1024, we resample patches used for fine-tuning. Other than that, we keep their original setup, which fine-tunes the mask decoder of the SAM 2 model and the memory layer, unchanged. We use the default configuration of one query point in every second slice for both training and inference.

10. Additional Qualitative Zero-Shot Results

To emphasize the exceptional *zero-shot* generalization of vesselFM, we present additional qualitative results achieved on all four evaluation datasets (see Figs. 13 to 16). Our findings demonstrate that vesselFM segments blood vessels very accurately across all evaluation datasets. Interestingly, vesselFM also segments tubular-appearing structures beyond blood vessels (*e.g.*, axons (see Fig. 15) or parts of the colon (see Fig. 14)). This highlights vesselFM’s strong inductive bias towards tubular shapes.

By segmenting all tubular structures in the volume, vesselFM segments structures, which are, at least to some degree, not annotated in ground truth labels (*e.g.*, aorta or other components of the systemic arterial circulation in MSD8 (see Fig. 14)). We argue that this may artificially deflate vesselFM’s quantitative results reported for the *zero-shot* task in Table 2.

11. More Samples From $\mathcal{D}_{\text{drand}}$ and $\mathcal{D}_{\text{flow}}$

We present additional samples from $\mathcal{D}_{\text{drand}} = \{\mathcal{X}_{\text{drand}}, \mathcal{M}_{\text{syn}}\}$ and $\mathcal{D}_{\text{flow}} = \{\mathcal{X}_{\text{flow}}, \mathcal{M}_{\text{syn}}\}$ in Fig. 11a and b, respectively. In conclusion, one can state that our domain randomized generative pipeline produces a wide variety of image-mask pairs with highly diverse fore- and background geometries and textures, while images sampled from our flow matching-based generative model \mathcal{F} exhibit intensity patterns closely mimicking those of real images in $\mathcal{D}_{\text{real}}$.

12. Additional Flow Matching Trajectories

Fig. 8 presents additional sampled flow matching trajectories, similar to Fig. 5. Specifically, we visualize the mapping from $x_0 \sim \mathcal{N}(0, I)$ to samples x_1 of exemplary classes indicated in red.

13. More Masks \mathcal{M}_{syn}

To further showcase the wide variety of synthetic masks \mathcal{M}_{syn} produced by our proposed domain randomized generative pipeline, we present a comprehensive selection in Fig. 12. Masks contained in \mathcal{M}_{syn} encompass a broad range

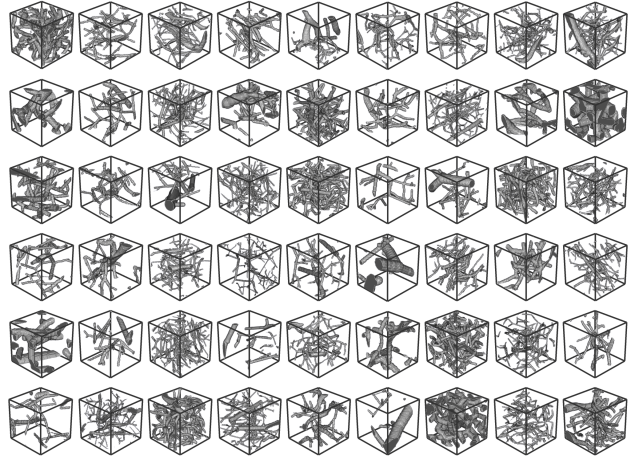


Figure 12. More exemplary synthetic masks \mathcal{M}_{syn} , generated by our proposed domain randomized generative pipeline (see Fig. 4a).

of realistic vascular patterns, capturing variations in blood vessel scale, density, curvature, and tortuosity.

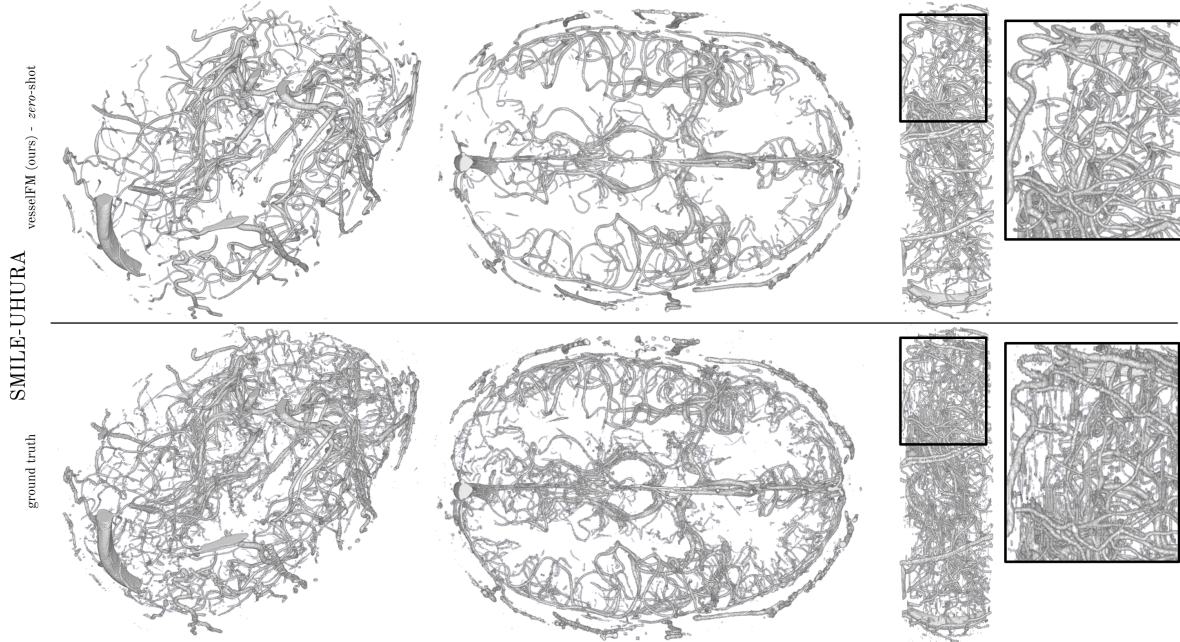


Figure 13. Qualitative results achieved on an exemplary test sample from the SMILE-UHURA dataset [9]. We compare vesselFM’s prediction in the *zero-shot* setting (top row) to the ground truth label contained in the SMILE-UHURA dataset (bottom row). VesselFM delivers remarkable results free of artifacts and accurately maintains the tubular appearance of blood vessels (see black box).

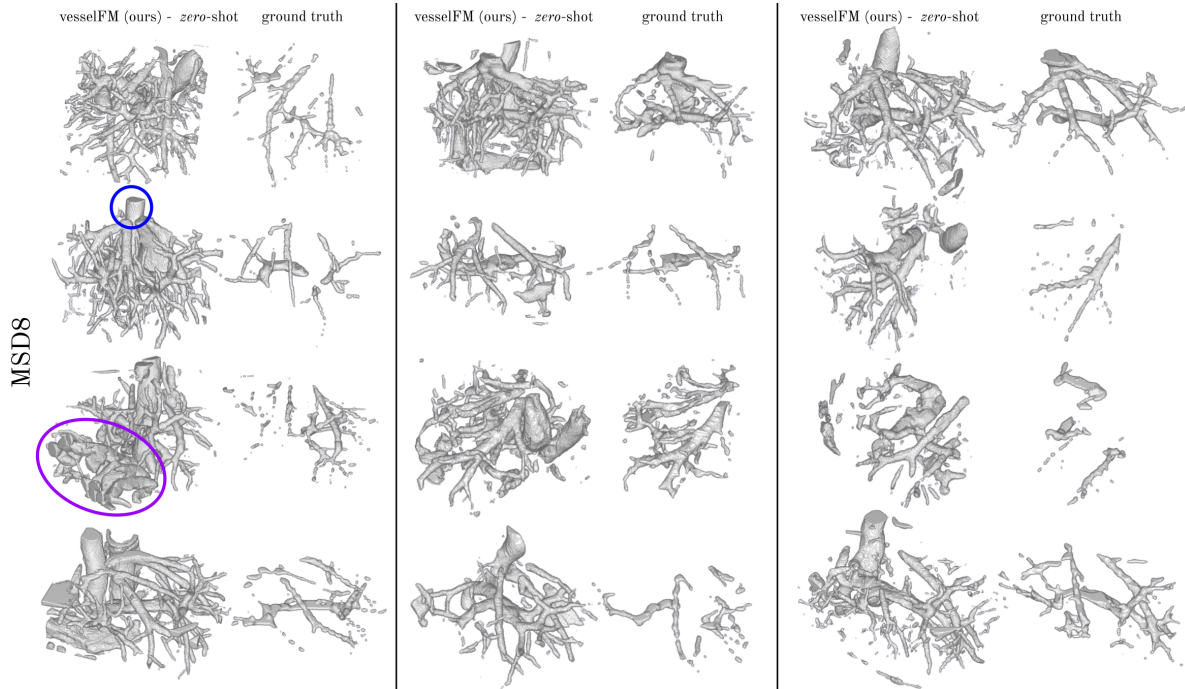


Figure 14. Qualitative results achieved on multiple test samples from the MSD8 dataset [2]. We compare vesselFM’s predictions in the *zero-shot* setting to ground truth labels for the task of hepatic vessel segmentation contained in the MSD8 dataset. VesselFM accurately segments all blood vessels (*e.g.*, aorta (marked in blue) and other major components of the systemic arterial circulation) and even other tubular structures (*e.g.*, the colon (marked in purple) and parts of the rib cage) present in CT scans.

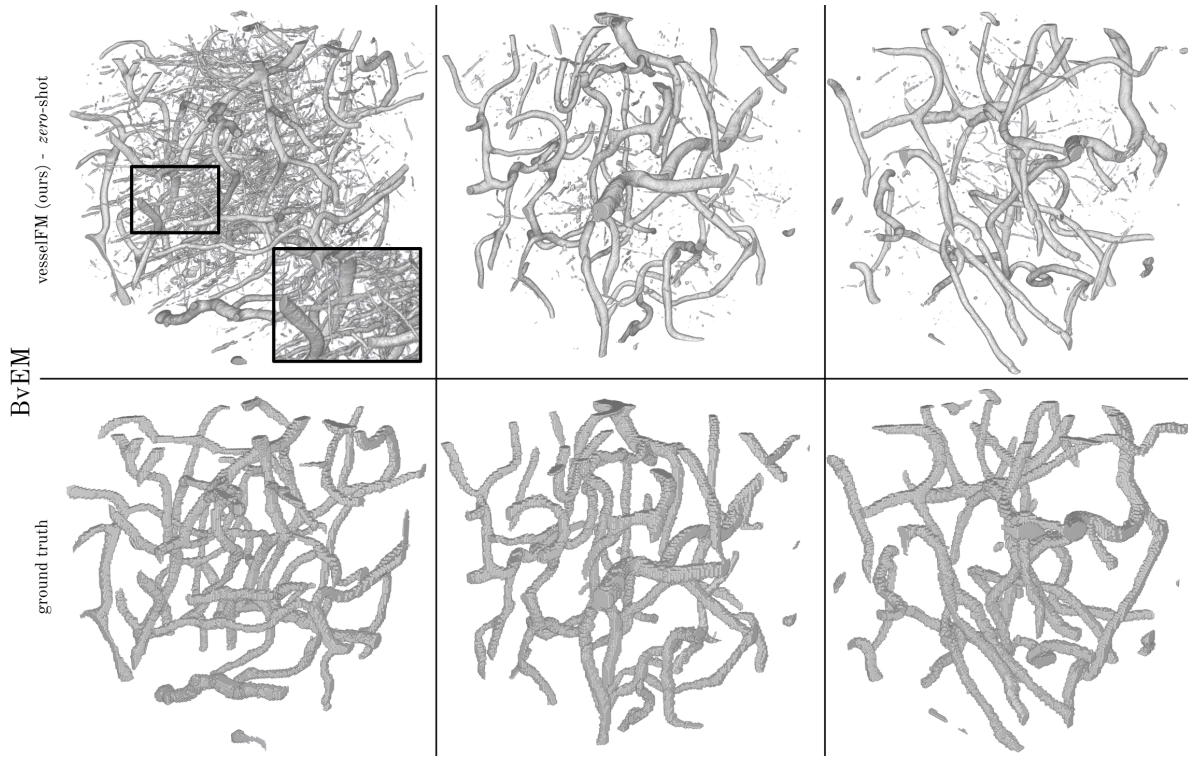


Figure 15. Qualitative results achieved on the three test volumes extracted from the BvEM dataset [51]. We compare vesselFM’s predictions in the *zero-shot* setting (top row) to ground truth labels contained in the BvEM dataset (bottom row). We find that vesselFM segments murine cortical vasculature contained in volume electron microscopy (vEM) images very precisely. Interestingly, vesselFM segments not only blood vessels but also tubular-appearing axons and even dendrites of pyramidal cells (see black box) visible in vEM images [11].

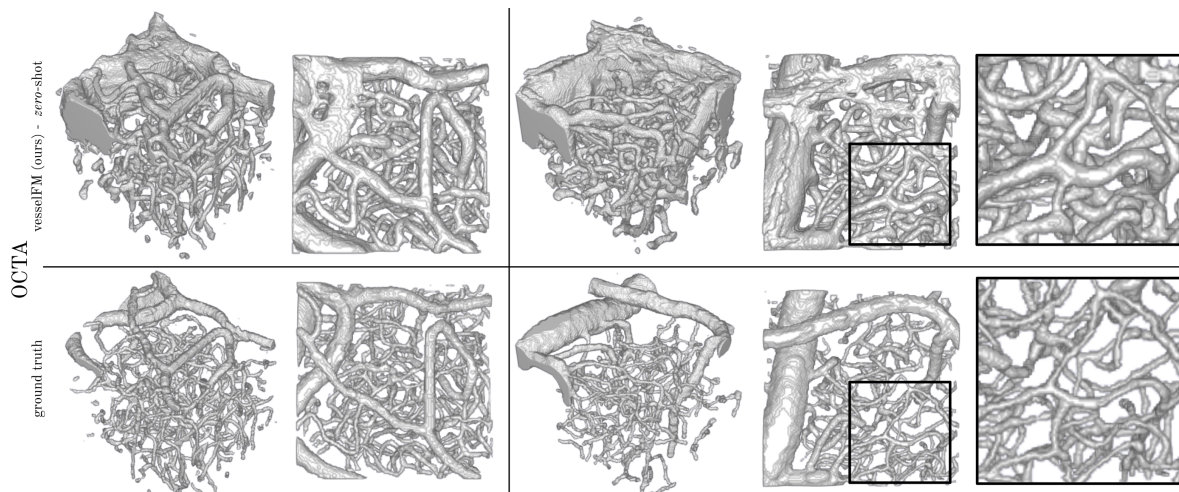


Figure 16. Qualitative results achieved on two test samples from the OCTA dataset [17, 54]. We compare vesselFM’s predictions in the *zero-shot* setting (top row) to ground truth labels contained in the OCTA dataset (bottom row). Although OCTA images are known for being plagued by dominant imaging artifacts [25, 31, 60], vesselFM still manages to segment densely connected vasculature (see black box).